JMEPEG (2024) 33:6362–6371
https://doi.org/10.1007/s11665-024-09490-8

1059-9495/$19.00

ORIGINAL RESEARCH ARTICLE

Scratch Properties of Nb Ion-Implanted WC-Ni Cold Sprayed Coatings

P. Nunthavarawong and N. Sacks

Submitted: 10 December 2023 / Revised: 5 March 2024 / Accepted: 13 March 2024 / Published online: 3 May 2024

The effect of niobium ion implantation on the surface and scratch properties of a WC-5wt.%Ni cold sprayed coating was investigated with accelerating energies of 60 and 170 keV and fluences of 5 × 10^{16} and 8 × 10^{16} ions cm^{-2}, respectively. High-resolution Rutherford backscattering spectroscopy spectra revealed that Ni-Nb and WC-Nb amorphous layers had likely formed. Using ion implantation parameters of 60 keV with a fluence of 8 × 10^{16} ions cm^{-2} (coating 608-NB), higher Nb peak intensities were found. Oxide formation in the form of NbO, NbO_2, and Nb_2O_5 was detected with high-resolution x-ray photoelectron spectroscopy spectra analyses on the 608-NB coating, in conjunction with the intermetallic, thereby having the best coating properties: higher hardness, low roughness, and scratch properties compared to the other ion-doped samples. The failure mechanisms of all the coatings were found to be similar, showing angular cracks, cone cracking, and primary delamination.

Keywords coating, cold spray, ion implantation, Nb, scratch test, WC-Ni

1. Introduction

The use of ion implantation surface treatments onto metals and ceramics has been performed over several decades to enhance oxidation and wear resistance, as well as increasing material lifespan. Metal ions such as W^+, Ta^+, Mo^+, Ru^+, and Nb^+ have been successfully deposited into metal and ceramic substrates, with the ions penetrating the substrate material, resulting in higher hardness, corrosion, and wear resistances (Ref 1-3). It has also been shown that ion radiation at non-optimal implantation energies may adversely affect the surface topography of the substrate material and can cause surface roughening.

To date, research into the use of Nb^+ ion implantation into aluminum and titanium-based coatings has yielded better coating properties such as higher hardness, high temperature oxidation resistance (Ref 2), and improved sliding wear properties (Ref 1, 5, 6). In these studies, the ion radiation was done using an accelerating energy ranging from 40 to 180 keV and fluences of 1 × 10^{16} to 8 × 10^{17} ions cm^{-2} (Ref 5-9). Furthermore, niobium ions in intermetallic compounds have shown good mechanical and tribological properties, especially for high-temperature oxidation resistance where superior properties over Cr and Mn intermetallic alloys were observed (Ref 10). Thus, in the current study, the effect of Nb^+ ion implantation into cemented tungsten carbide–nickel (WC-Ni) cold sprayed coatings was investigated. Cemented tungsten carbide coatings are employed extensively in the manufacturing and mining industries where they provide improved hardness and wear resistance to both tooling and wear parts. These coatings are typically produced using high-temperature deposition methods such as high-velocity oxy-fuel (HVOF), wherein the coatings often experience undesirable characteristics such as thermal oxidation, phase transformations, carbide grain growth, and even tensile residual stresses (Ref 11).

Alternatively, cold sprayed coatings, which employ much lower deposition temperatures, have shown the absence of these undesirable traits. However, there are some disadvantages of cold sprayed cemented carbide coatings which need to be overcome before they can become commercially competitive with their high temperature counterparts. These disadvantages include a low retention of the WC phase in the coating and erosion of the substrate as well as formerly deposited layers by the WC particles during spraying (Ref 12-17). The hard, brittle WC particles may also crack during deposition, which can lead to a decreased coating hardness and strength (Ref 16). Research has been done to improve the coating properties by adding Mo (Ref 43) and TiC particles (Ref 15) to the feedstock powders, and some improvements have been achieved. Thus far, the influence of Nb^+ ion implantation on the surface properties of cemented tungsten carbide cold sprayed coatings has not been investigated. Therefore, in the current research study the influence of Nb^+ ion implantation into WC-5wt.%Ni cold sprayed coatings was investigated by assessing the effects of Nb^+ ion accelerating energy and fluence on the coating surface properties.

P. Nunthavarawong, (Formerly) School of Chemical and Metallurgical Engineering, University of the Witwatersrand, Private Bag 3, Wits 2050, South Africa; DSI-NRF Centre of Excellence in Strong Materials, Johannesburg, South Africa; and Tribo-Systems for Industrial Tools and Machinery Research Laboratory, The Sirindhorn International Thai-German Graduate School of Engineering, King Mongkut's University of Technology North Bangkok, 1518 PrachaRat 1 Rd., Wongsawang, Bang-Sue, Bangkok 10800, Thailand; and **N. Sacks**, DSI-NRF Centre of Excellence in Strong Materials, Johannesburg, South Africa; and Department of Industrial Engineering, Stellenbosch University, Private Bag X1, Matieland 7602, South Africa. Contact e-mail: peerawatt.n@tggs.kmutnb.ac.th.

2. Materials and Methods

2.1 Materials

2.1.1 Cermet Substrates. The WC-5wt.%Ni coatings, denoted as 5-WN in this paper, were deposited onto 3CR12 stainless steel plates (20 × 20 × 3 mm) using a low-pressure cold spray machine (Centerline SST Series P, Canada). The 5-WN coatings were produced using optimum spraying parameters determined in an earlier study (Ref 16), where coatings at least 400 μm-thick were produced with a small WC grain size (0.57 ± 0.30 μm), a low Ni binder mean free path (0.07 ± 0.002 μm), a high WC retention in the coating (43 ± 5 wt.%), and a low porosity (0.55 ± 0.08 %). Samples were ground using standard metallographic procedures, polished to a 1 μm surface finish, and then ultrasonically cleaned prior to ion implantation.

2.1.2 Implanted Coatings. Niobium (99.9%, sputtering target, Goodfellow, U.K.) ions were implanted into the 5-WN cermet coatings using two different accelerating energies, namely 60 (Ref 18) and 170 keV, at two different fluences of 5 x 10^{16} and 8 x 10^{16} ions cm^{-2}, respectively, using a 200-20A2F ion implanter (iThemba LABS, South Africa), in order to investigate the influence of the ion deposition parameters on the resultant coating properties. The as-implanted coatings are denoted as 605-NB, 608-NB, 1705-NB, and 1708-NB, respectively. The operating temperature during ion implantation was controlled at room temperature.

2.2 Material Characterization

2.2.1 Rutherford Backscattering Spectrometry (RBS). An RBS technique (iThemba LABS, South Africa) was used to determine the compositions of the implanted layers, coupled with OMDAQ-3 software used for elemental analysis. The $^{4}He^{++}$ incident was undertaken at 3.6 MeV with ion incident settings of beam size diameters of 1-10 μm, a scattering angle of 150°, an exit angle of 30°, and a detector-to-specimen distance of 25 mm. This was coupled with microprobe beam settings of 0.1 μC, 0.25 nA, and a counting rate of 0.398 kHz, detected by using a Canberra PIPS® sensor over a 150 mm^2 scan area.

2.2.2 X-ray Photoelectron Spectroscopy (XPS). The chemical bonding state of the implanted coatings was identified using XPS (Thermo ESCALAB 250Xi, Thermo Fisher Scientific Inc., U.S.A.), with an x-ray generator setting of 900 W, coupled with a monochromatized Al-Kα radiation setting at 1486.68 eV. The binding energies were referenced to the C1s peak at 284.6 eV. In order to identify the phase compositions produced in the ion-implanted samples, peak fitting of the high-resolution XPS spectra was computed using the Shirley background method by means of XPSPEAK software (Ref 19).

2.2.3 Scanning Electron Microscopy (SEM). Field emission SEM (FE-SEM, Carl Zeiss Sigma, Germany) was used to characterize the coating surfaces in secondary electron (SE) and backscattered electron (BSE) imaging modes.

2.2.4 Atomic Force Microscopy (AFM). An AFM (Dimension 3100, Digital Instruments Inc., U.S.A.), coupled with Nano Scope Analysis software (Bruker Corporation, U.S.A.), was employed to characterize the surface topography and to measure the surface roughness of the coatings, both as-ion-implanted and non-ion-implanted. The scanning area was fixed at 25 μm^2 (256 × 256 pixels) for each measurement in tapping mode, with the etched silicon probe at 1.0 Hz of the scan rate applied (tip radius = 8 nm, resonance frequency = 75 kHz, and spring constant = 2.8 N m^{-1}). The average surface roughness (Ra) and the root mean square deviation of the assessed roughness profile (Rq), were determined at the fixed position over the four corners and the center (15 points) of each sample, according to ISO 4287 (Ref 20, 21).

2.3 Hardness and Scratch Tests

2.3.1 Hardness Tests. Micro-Vickers hardness tests (Future tech FM-700, Japan) were done on the planar surfaces of the ion-implanted layers and the cermet coatings using a 50 gf indenting load, with a 10 s dwell time, according to ASTM C1327 (Ref 21).

2.3.2 Scratch Tests. A Revetest Scratch Tester (Anton Paar TriTec, Switzerland), coupled with a Rockwell-C diamond as the stylus probe (tip radius = 200 μm), was used to evaluate the scratch properties and failure mechanisms of the ion-implanted and non-ion-implanted coatings. A progressive-load scratch test (PLST), coupled with Scratch software version 4.52, was used to determine the critical loads (L_{Cx}) according to ISO 20502 (Ref 22), when using parameter settings of 1-100 N applied loads, a loading rate of 99 N min^{-1}, a sliding speed of 10 mm min^{-1}, and a sliding distance of 10 mm. The critical delamination stress at the point where the coating was peeling from the substrate (σ_D) was determined using Eq 1 (Ref 23), where L_{C3}, W_{C3}, ν_i, and μ are the maximum critical load due to the delamination failure, the scratch track width at L_{C3} determined using FE-SEM images, Poisson's ratios of 5-WN (ν_i = 0.22) and Nb film (ν_i = 0.4), and the friction coefficient of the coatings as recorded by the scratch instrument at a high friction state.

$$\sigma_D = (2L_{C3}/\pi w_{C3}^2)\left[((4+\nu_i)\,3\pi\mu/8) - (1-2\nu_i)\right] \quad \text{(Eq 1)}$$

The toughness was also evaluated using the scratch test (T_{ST}) and was calculated using Eq. 2 (Ref 24, 25), where L_{C1} is the minimum critical load at initial cracking (angular cracks). The remaining critical loads defined by the critical load due to the initial cone cracks on the scratch track (L_{C2}) were also measured.

$$T_{ST} = L_{C1}(L_{C3} - L_{C1}) \quad \text{(Eq 2)}$$

An incremental-load scratch test (ILST), with applied loads of 1 - 15 N at 5 N load increments, a sliding speed of 10 mm min^{-1}, and a sliding distance of 6 mm, was used to evaluate the transition load to failure.

3. Results and Discussion

3.1 Surface Characterization and Analyses

Figure 1(a) illustrates the RBS spectra of the as-implanted coatings, whereby the C, O, Ni, Nb, and W elements were measured. From high-resolution analyses of the RBS spectra (refer Fig. 1b), it was found that each coating showed the Nb peak in between the Ni and W peaks, thereby indicating the formation of a Ni-Nb-WC intermetallic compound. For the 608-NB specimens, the RBS spectra showed higher Nb peak intensities at 3,067 keV compared to the other three coatings.

To increase the understanding of the elemental distributions in the ion-implanted coatings, high-resolution XPS spectra of sample 608-NB were obtained, with the results shown in Fig. 2. The $Nb3d_{5/2}$ peaks were detected as shown in Fig. 2(a). The binding energy of the $Nb3d_{5/2}$ core level at the first peak had a value of 203.68 eV, thereby implying that niobium oxide (NbO) had formed (Ref 19), while the transitional spectrum had a peak value of 205.65 eV, identifying as niobium dioxide, NbO_2 (Ref 19). The third peak had a value of 206.57 eV, identifying as the $Nb3d_{5/2}$ spectral line for niobium pentoxide, Nb_2O_5 (Ref 26). The analyses of the nickel phase are shown in Fig. 2(b) for the Ni2p spectrum. The highest peak had a binding energy value of 853.36 eV, identifying as $Ni2p_{3/2}$ for pure nickel, and the lower peak had a value of 870.24 eV, identifying as $Ni2p_{1/2}$ for pure nickel (Ref 26); the difference of the two peaks was 16.88 eV.

The AFM analysis evaluated surface roughness profiles for all coatings, including the non-ion-implanted one (see Fig. 3). The surface roughness values are shown in Table 1. A lower Rq and Ra were obtained for the 608-NB specimens with values of 9.09 ± 1.04 nm and 7.16 ± 0.80 nm, respectively, compared to the other coatings. The non-ion-implanted cermet coating had the highest surface roughness values. These findings could be attributed to the fact that the ion dopant at high fluence and low accelerating energy produced a smoothening of the surface, also mentioned by (Ref 27).

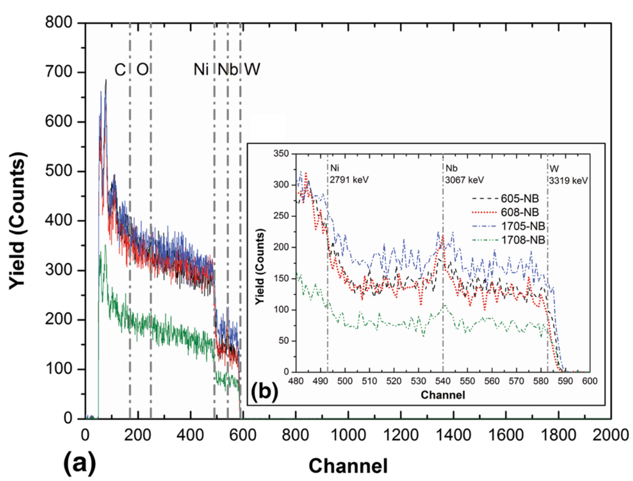

Fig. 1 RBS analyses of the as-implanted coatings. (a) Wide scan spectra of element (b) high-resolution scan spectra of the Ni, Nb, and W

3.2 Hardness and Scratch Test Results

As seen in Fig. 2, oxides are present in niobium, probably due to post-implantation exposure to atmospheric conditions. These oxides might contribute to the increased hardness of ion-implanted coatings compared to non-implanted ones (see Table 1). Also, the 608-NB Nb ion-implanted coating produced higher hardness values (556 ± 25 $HV_{0.05}$) compared to the other four coatings, as seen in Table 1, with a 30% increase compared to the non-implanted cermet coating. When the accelerating energy was increased from 60 to 170 keV, the higher associated temperature increased during implantation created a thermal annealing effect (Ref 7), resulting in a decrease of the hardness for the 1705-NB and 1708-NB samples. Figure 4 represents the coefficient of friction as a function of applied load during the scratch tests. The evolution of friction for all coatings can be assigned to three distinct regimes, namely low friction (1.1-26 N), transition friction (26.1-50 N), and high friction (50.1-100 N), respectively. The curves obtained in the low friction state showed similar behavior for the 5-WN and 1708-NB samples, while the remaining three coatings showed a friction peak toward the end of the low friction regime before entering the transition zone. In the transition friction state, the 608-NB coating showed an overall lower friction response as the load increased up to 45 N after which its friction behavior was comparable to some of the other coatings. This coating had the highest hardness, and it was thus interesting that its overall friction response was not the severest among all the coatings. The 1708-NB coating produced the highest friction response in the high friction regime with average values of 0.662 ± 0.05, compared to the other four coatings, as listed in Table 2.

Figure 5 and 6 illustrate the penetrating depth profiles for each coating as measured during the scratch test as a function of applied load. At high progressive loads in PLST testing (1 - 100 N), as shown in Fig. 5, the penetration depth increased as the applied load increased. The profiles are generally linear in nature until about 40 N, after which some nonlinear deviations initiate. The deviations from linearity for the two coatings 1705-NB and 1708-NB, implanted with the higher 170 keV accelerating voltage, are greater than those of the remaining

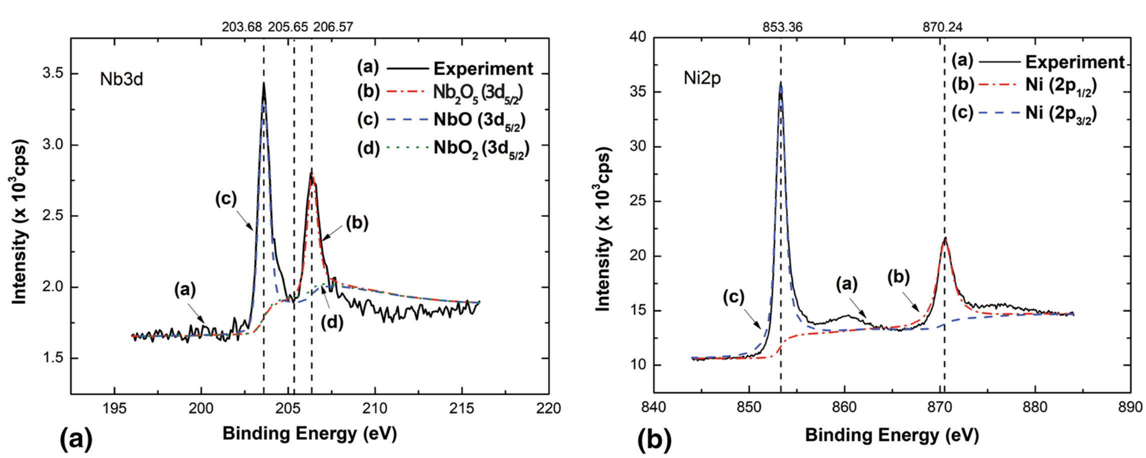

Fig. 2 High-resolution XPS spectra analyses of 608-NB. (a) Nb and (b) Ni

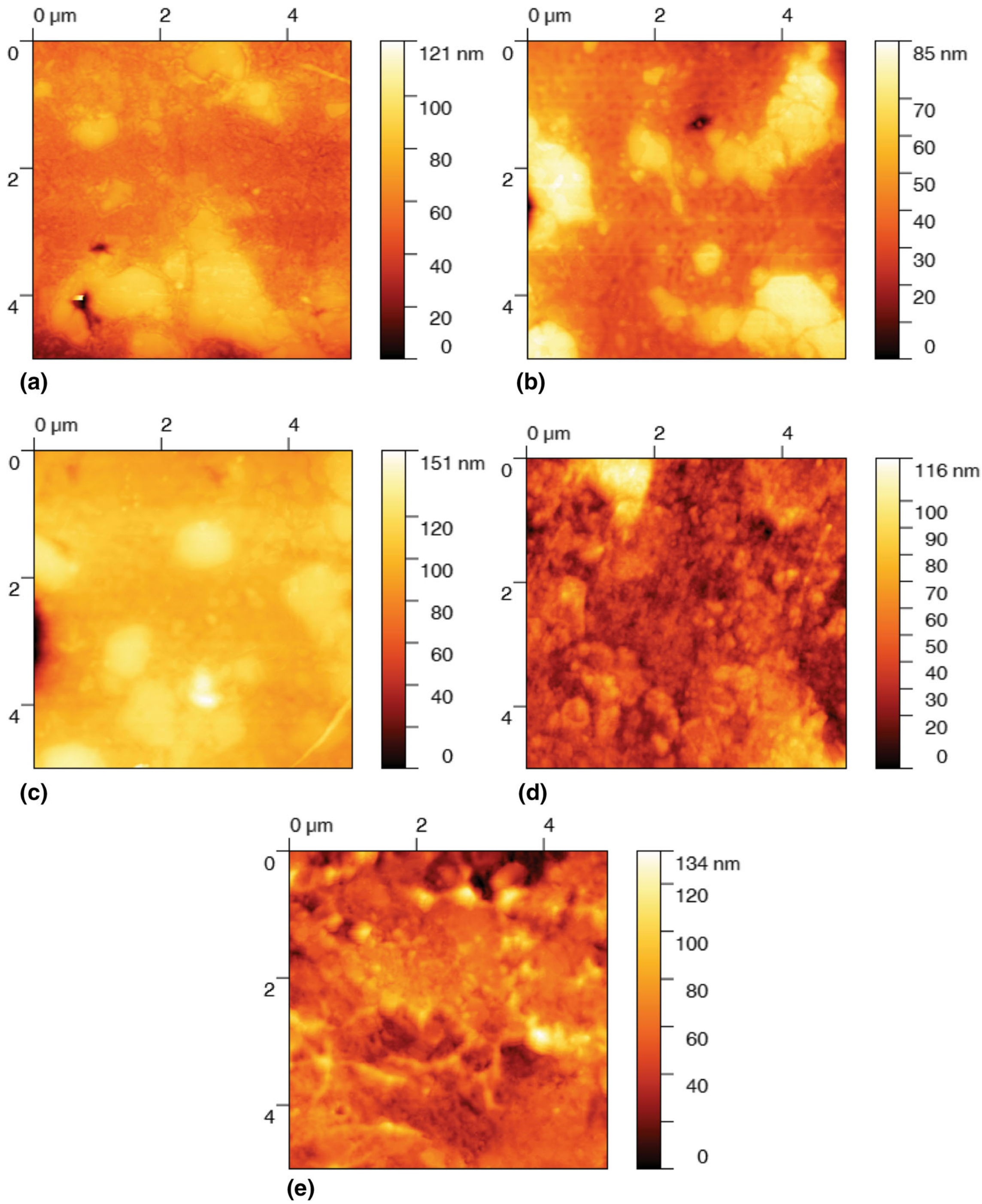

Fig. 3 AFM images of the un-implanted and as-implanted coatings. (a) 5-WN (b) 605-NB (c) 608-NB (d) 1705-NB and (e) 1708-NB. Bright phase = WC, color phase = Ni and/or Nb, dark phase = defect

Table 1 Roughness and hardness of the coatings

	Material				
Parameter	**5-WN**	**605-NB**	**608-NB**	**1705-NB**	**1708-NB**
Rq, nm	21.10 ± 13.94	11.05 ± 1.29	9.09 ± 1.04	14.30 ± 3.17	13.50 ± 5.44
Ra, nm	15.41 ± 7.38	8.98 ± 2.21	7.16 ± 0.08	11.27 ± 2.22	13.94 ± 1.99
Hardness, $HV_{0.05}$	425 ± 34	537 ± 29	556 ± 25	517 ± 21	533 ± 17

three coatings, especially when reaching an applied load of 70 N, indicating progressively greater surface damage. These two coatings also achieved deeper penetration depths at the final applied load of 100 N of 47 and 49 μm, respectively, while the 5-WN, 605-NB and 608-NB coatings had values of 32, 43 and 37 μm, respectively. At low multi-step applied loads during the ILST testing (1-15 N; cf. Fig. 6), the 5-WN coating experienced a lower penetration depth compared to the four implanted coatings even though it is less hard than the implanted coatings; this implies that ion implantation may produce a more brittle structure which is more prone to surface cracking. Despite the lower penetration depth of the non-implanted coating, it did not achieve the best strength properties as shown in Table 2. Rather the 608-NB Nb ion-implanted coating showed the best strength properties. It had a smaller scratch track (W_{C3} = 106 ± 1 μm), good friction response during the high friction state (μ_{high} = 0.611 ± 0.02), higher average critical load (L_{Cavg} = 48.6 N), higher critical delamination strength (σ_D = 11.2 ± 0.3 GPa), and optimum toughness properties (T_{ST} = 1067 N^2). This latter coating also showed a 27% lower sliding wear rate compared to the 605-NB coating, as reported in earlier research (Ref 18).

Overall, the influence of Nb ions on scratch test results can vary depending on the specific loading conditions. As the presence of Nb ions could improve performance, higher energy remarkably exhibited severe surface damage compared to the cold sprayed coating implanted at lower accelerating voltage,

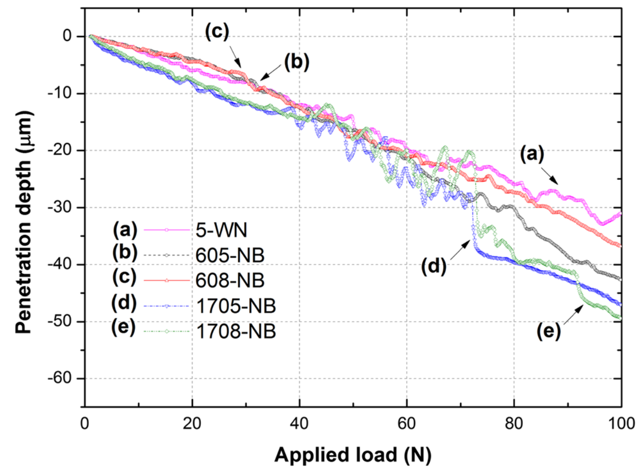

Fig. 5 Penetration depth response as a function of progressive loads of 1 - 100 N. (a) 5-WN (b) 605-NB (c) 608-NB (d) 1705-NB and (e) 1708-NB

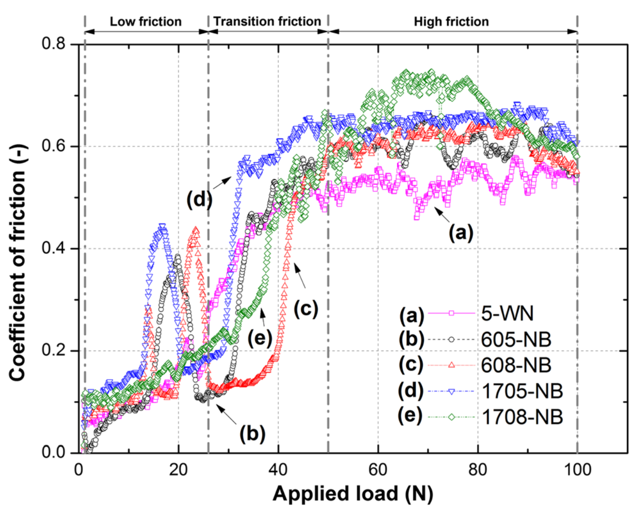

Fig. 4 Friction response as a function of progressive loads of 1 - 100 N. (a) 5-WN (b) 605-NB (c) 608-NB (d) 1705-NB and (e) 1708-NB

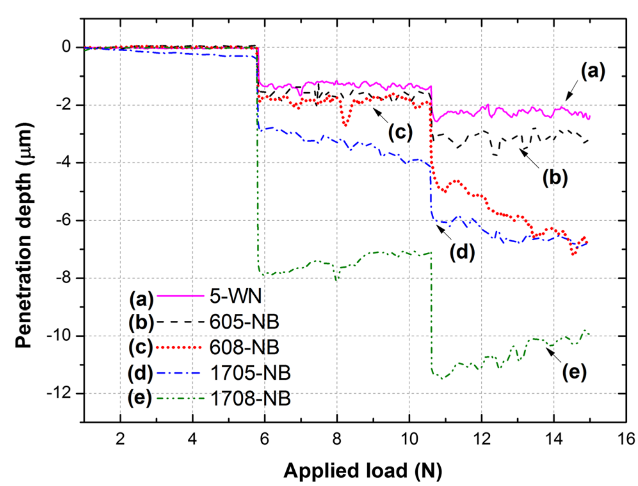

Fig. 6 Penetration depth response as a function of multi-step loads of 1 - 15 N. (a) 5-WN (b) 605-NB (c) 608-NB (d) 1705-NB and (e) 1708-NB

Table 2 Strength and scratch properties of the coatings

Parameter	Material				
	5-WN	**605-NB**	**608-NB**	**1705-NB**	**1708-NB**
L_{C1}, N	17.5	29.7	26.0	28.1	20.4
L_{C2}, N	33.8	45.0	52.6	39.6	26.3
L_{C3}, N	63.7	69.0	67.0	59.4	63.6
L_{Cavg}, N	38.3	47.9	48.6	42.4	36.7
W_{C3}, μm	118 ± 3	112 ± 3	106 ± 1	116 ± 4	139 ± 9
Friction coefficient at high friction state, μ_{high}, -	0.532 ± 0.02	0.604 ± 0.03	0.611 ± 0.02	0.647 ± 0.02	0.662 ± 0.05
Critical delamination strength, σ_D, GPa	6.1 ± 0.3	10.2 ± 0.6	11.2 ± 0.3	8.9 ± 0.6	6.8 ± 0.9
Toughness property, T_{ST}, N^2	809	1166	1067	880	881

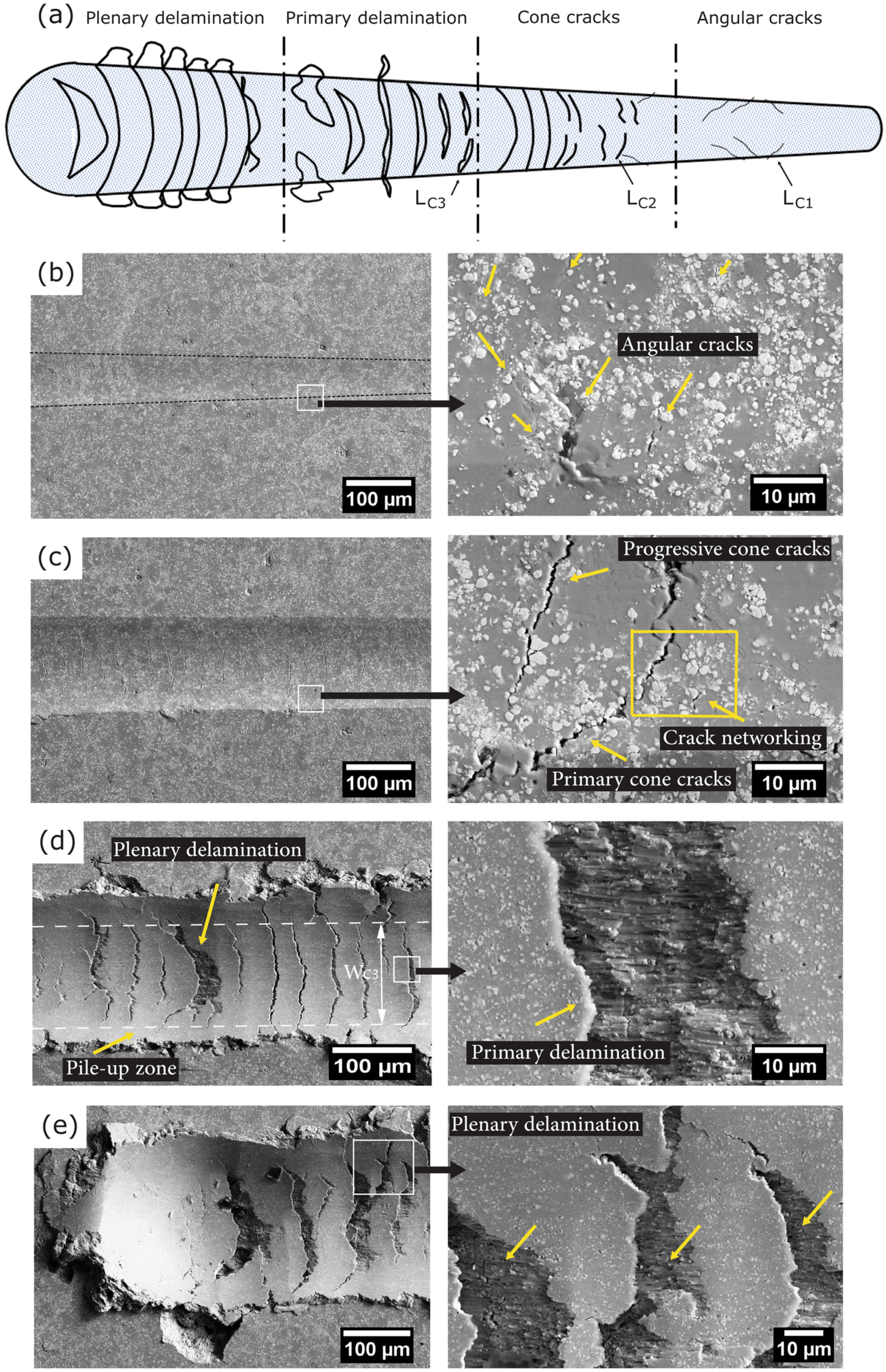

Fig. 7 (a) Failure maps of 1708-NB. FE-SEM images of 1708-NB showing failure mechanisms of (b) angular cracks discovered at the edge of the scratch track, (c) cone cracks observed, (d) primary and plenary delaminations discovered, and (e) plenary delamination observed

resulting in deeper scratch depths or increased material removal. The results of penetrating depth profiles during scratch tests are depicted, showing variations with applied load for different coatings. In high-load PLST testing, coatings 1705-NB and 1708-NB, implanted with higher accelerating voltage, exhibit greater deviations and deeper penetration depths than 5-WN, 605-NB, and 608-NB coatings. In low-load ILST testing, 5-WN coating shows lower penetration depth than implanted coatings, despite being less hard, suggesting ion implantation may induce a more brittle structure prone to surface cracking. Notably, the 608-NB coating, despite deeper penetration depth, exhibits greater strength properties

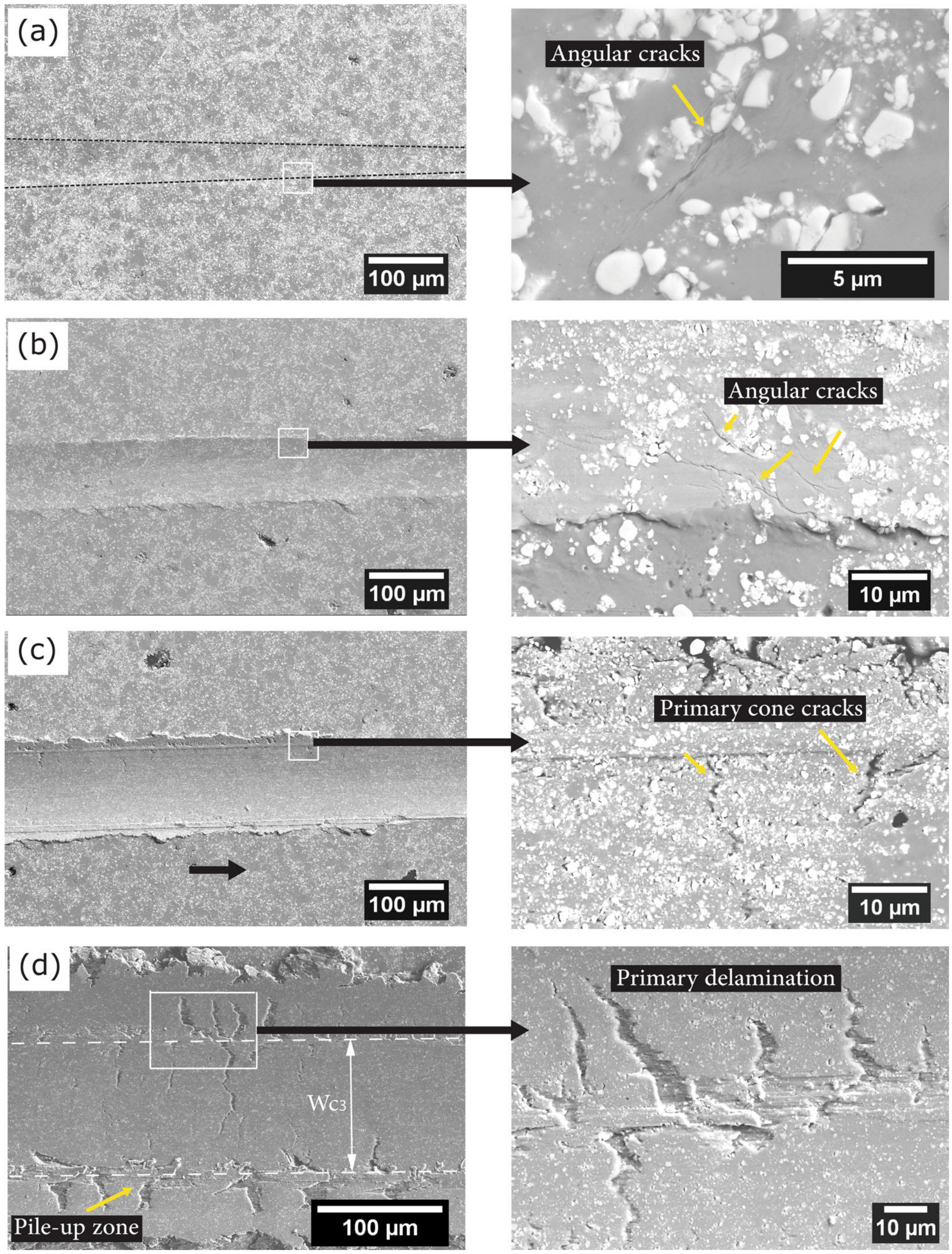

Fig. 8 FE-SEM images of 608-NB showing failure mechanisms of (a and b) angular cracks discovered at the edge of the scratch track, (c) cone cracks observed, and (d) primary delamination discovered

compared to 605-NB, indicating ion implantation's beneficial effects on mechanical performance.

3.3 Failure Mechanisms

The failure mechanisms experienced during the scratch tests were examined, and the resultant images are shown in Fig. 7 for the 1708-NB coating, Fig. 8 for the 608-NB coating, and Fig. 9 for the 5-WN coating. A schematic depicting the main failure mechanisms observed in the coatings as the applied load increased is shown in Fig. 7(a) and is explained as follows:

(1) Angular cracks: In the zone of the initial loads (1-25 N), the first angular crack is defined as L_{C1}, which was observed at the edge of the scratch tracks; this aligns with similar observations found in thermally sprayed WC-CoCr coatings (Ref 29). The angular cracks were generated by the two tensile stresses present during testing, namely the tensile stress toward the scratch direction and tensional stress across the scratch groove (Ref 28). In the current study, the types of angular cracks can be divided into a backward angular crack (i.e. crack path produced in front of the moving blunt tip) and a forward angular crack (i.e. crack path produced behind the moving blunt tip) when compared to the scratch direction, in which the high plastic deformation of the ductile phase (Ni and/or Nb) induced the crack paths

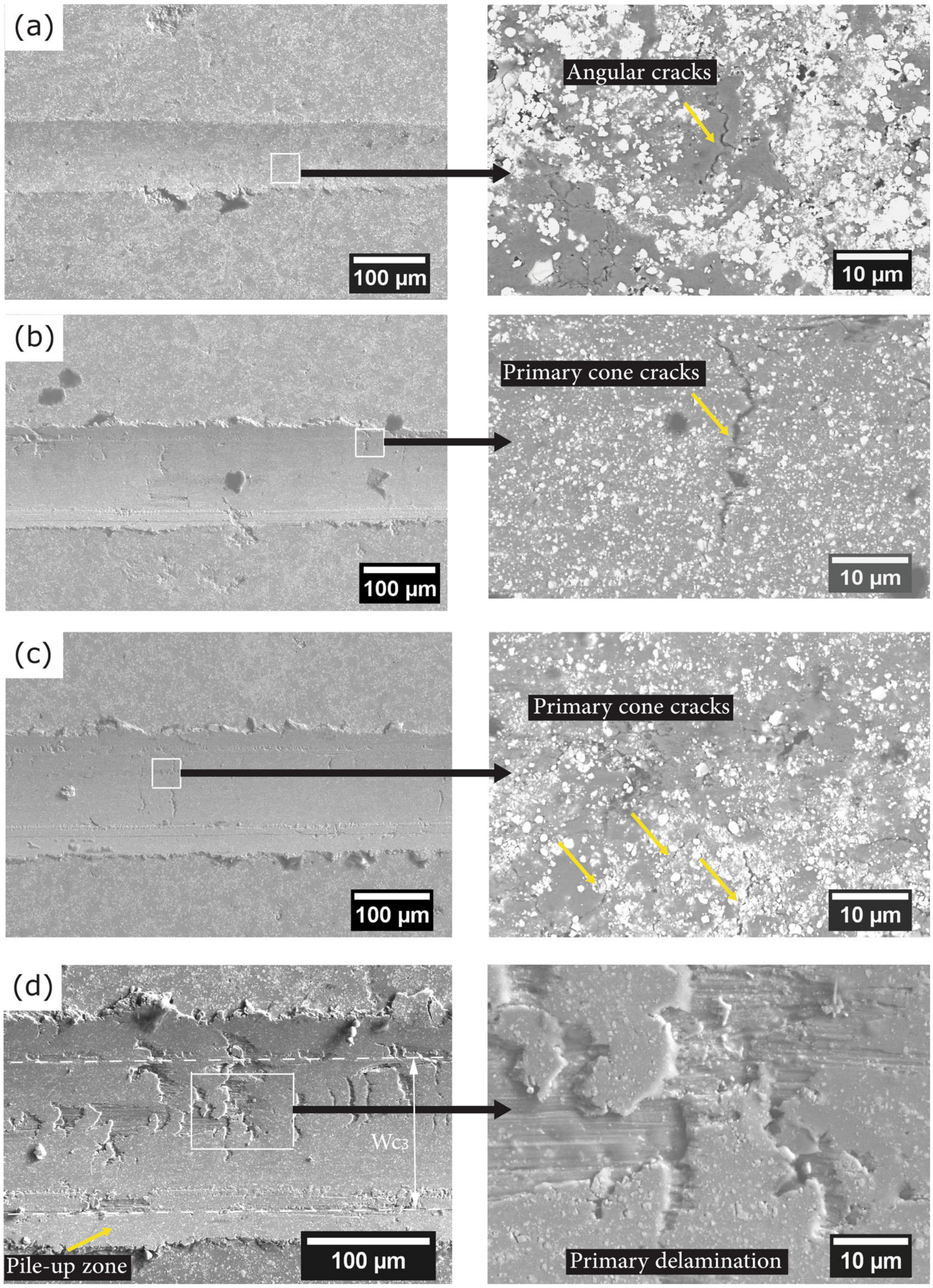

Fig. 9 FE-SEM images of 5-WN showing failure mechanisms of (a) angular cracks discovered at the edge of the scratch track, (b and c) cone cracks observed, and (d) primary delamination discovered

through the edge of the scratch tracks in the two directions. The angular cracks are associated with ductile failure as they were mainly observed at the interface between the WC and the ductile binders, as illustrated in Fig. 7(b) and Fig. 8(a) and (b) for 608-NB and Fig. 9(a) for 5-WN, respectively.

(2) Primary cone and progressive cone cracks: Primary cone and progressive cone cracks were observed during the applied loads of 25 - 50 N. In this state a sudden increase of sliding friction (transition friction) at the higher load (see Fig. 4) induced higher tensile stresses beneath the coating surface, in which the cone cracks were formed around the tail of the moving blunt tip. The primary cone crack (L_{C2}) is due to the lower initial load where the slight increase in pressure leads to the initial cracks being formed within a short length (see Fig. 8(c) for 608-NB and Fig. 9(b) and (c) for 5-WN). When the progressive load increases to a high magnitude, the radial cracks may propagate higher across the scratch track (Ref 29), and thus, any initial cracking experienced by the WC particles during the cold spray deposition process is then further propagated in random directions causing a network of crack patterns, as seen in Fig. 7(c). Nevertheless, the progressive cone cracks

did not appear in the 5-WN (cf. Fig. 9) and the other three implanted coatings.

(3) Primary delamination (L_{C3}): At a higher load of around 75 N, the cone cracks are experiencing higher tensile stresses, and these cracks were seen to predominantly develop around the WC and binder splat boundaries. Excessive failure would then occur when detachment occurs due to increasing cone cracks, thereby causing primary delamination due to a weakened boundary between the Ni binder and WC particles (Ref 29), as can be seen in Fig. 7(d), 8(d) for 608-NB and Fig. 9(d) for 5-WN, respectively.

(4) Plenary delamination: At the highest loading zone, up to 100 N, excessive delamination occurs across the entire scratch track due to the increase in tensile stresses was observed, as shown in Fig. 7(e). This delamination failure propagates into the sub-surface layers, thereby resulting in a peeling effect by the coatings; however, this failure mode was not experienced in all the other coating samples, except 1708-NB. In this study, it should be noted that the severity of damage on the surfaces by the plenary delamination increased as the implantation energy and fluence increased (cf. Fig. 7d, e).

The failure mechanisms were similar for all coatings, namely angular cracks, cone cracking, and primary delamination. The degree of severity of the failure mechanisms increased with an increase in the accelerating voltage to 170 keV and the fluence to 8×10^{16} ions cm^{-2}.

4. Conclusions

Niobium ion implantation provided an overall improvement of the surface and scratch properties of the WC-5wt.%Ni cold sprayed coating, with an accelerating voltage of 60 keV and fluence of 8×10^{16} ions cm^{-2} producing the best coating properties. Using these parameters, a hardness of 556 $HV_{0.05}$ was achieved compared the original coating hardness of 425 $HV_{0.05}$, which is attributed to the formation of niobium oxide (NbO), niobium dioxide (NbO_2), and niobium pentoxide (Nb_2O_5) as well as the Ni-Nb-WC intermetallic. These implantation parameters also produced a coating with a low Rq roughness of 9.09 nm, low Ra roughness of 7.16 nm, smaller scratch track of 106 μm, lower friction response (0.611) during the scratch tests, higher average critical load (48.6 N), higher critical delamination strength (11.2 GPa), and good toughness properties (1067 N^2). The failure mechanisms experienced during the scratch tests were generally angular cracks, cone cracks, and primary delamination and were similar for all coatings, although the degree of severity increased with increasing accelerating voltage and fluence.

Acknowledgments

The authors wish to acknowledge the financial support received from the Department of Science and Innovation (DSI) and the National Research Foundation (NRF) in South Africa (Grant No: 41292). Opinions expressed and conclusions arrived at are those of the author(s) and are not necessarily to be attributed to the CoE-SM, DSI, or NRF. The authors acknowledge the technical support provided by Prof. Ionel Botef from the University of the Witwatersrand, South Africa.

Author Contributions

PN contributed to conceptualization, investigation, methodology, validation, formal analysis, writing—original draft, and visualization; NS performed writing—review and editing.

Funding

This research has received funding support from the Department of Science and Innovation (DSI) and the National Research Foundation (NRF) in South Africa (Grant no: 41292).

Data Availability

The data that support the findings of this study are available from the corresponding author, Peerawatt Nunthavarawong, upon reasonable request.

Conflict of interest

All authors declare that they have no known competing financial interests or personal relationships that could have appeared to influence the work reported in this paper.

References

1. M. Bauer, Ph. Kapsa, J.L. Loubet et al., Tribological Properties of Niobium Ion Implanted Alumina, *Tribol. Int.*, 1999, **25**, p 319–327
2. M.F. Stroosnijder, N. Zheng, W.J. Quadakkers et al., The Effect of Niobium Ion Implantation on the Oxidation Behavior of aγ-TiAl-Based Intermetallic, *Oxid. Met.*, 1996, **46**, p 19–35
3. C. Ringas, F.P.A. Robinson, S.B. Luyckx et al., Corrosion Behaviour of Ion Implanted WC-Co and WC-Ni Alloys in Acid and Chloride Containing Media, *Surf. Eng.*, 1990, **6**(3), p 194–198
4. W.L. Lin, J.M. Sang, X.J. Ding et al., Microchemical and Microstructural Changes of Co Cemented WC Induced by Ion Implantation, *Nucl. Instrum. Methods Phys. Res. Sect. B*, 2002, **188**, p 201–204
5. B. Deng, Y. Tao, H. Liu et al., Influence of Niobium Ion Implantation on the Microstructure and Tribological Properties of TiAlN Coatings, *Surf. Coat. Technol.*, 2013, **228**, p S554–S557
6. B. Liu, B. Deng and Y. Tao, Influence of Niobium Ion Implantation on the Microstructure, Mechanical and Tribological Properties of TiAlN/CrN Nano-Multilayer Coatings, *Surf. Coat. Technol.*, 2014, **240**, p 405–412
7. W. Miao, K. Tao, B.X. Liu et al., Formation of $NbAl_3$ by Nb Ion Implantation Using Metal Vapor Vacuum Arc Ion Source, *Nucl. Instrum. Methods Phys. Res. Sect. B*, 2000, **160**, p 343–348
8. Y.Z. Liu, X.T. Zu, S.Y. Qiu et al., Surface Characterization and Corrosion Resistance of Ti-Al-Zr Alloy by Niobium Ion Implantation, *Nucl. Instrum. Methods Phys. Res. Sect. B*, 2006, **244**, p 397–402
9. H.J. Schmutzler, N. Zheng, W.J. Quadakkers et al., The influence of Niobium Ion Implantation on the High Temperature Oxidation Behaviour of Ti-48Al-2Cr, *Surf. Coat. Technol.*, 1996, **83**, p 212–217
10. V.A.C. Haanappel and M.F. Stroosnijder, Ion Implantation Technique as Research Tool for Improving Oxidation Behaviour of TiAl Based Intermetallic Alloys, *Surf. Eng.*, 1999, **15**(2), p 119–125
11. S.M. Nahvi and M. Jafari, Microstructural and Mechanical Properties of Advanced HVOF Sprayed WC-Based Cermet Coatings, *Surf. Coat. Technol.*, 2016, **286**, p 95–102
12. N.M. Melendez, V.V. Narulkar, G.A. Fisher et al., Effect of Reinforcing Particles on the Wear Rate of Low-Pressure Cold-Sprayed WC-Based MMC Coatings, *Wear*, 2013, **306**, p 185–195

13. D. Lioma, N. Sacks and I. Botef, Cold Gas Dynamic Spraying of WC-Ni Cemented Carbide Coatings, *Int. J. Refract. Met. Hard Mater.*, 2015, **49**, p 365–373
14. N.B.S. Magagula, N. Sacks and I. Botef, Slurry Abrasion of WC-4wt%Ni Cold-Sprayed Coatings in Synthetic Minewater, *S. Afr. Inst. Min. Metal.*, 2016, **116**(4), p 333–337
15. N. Sacks, Low Pressure Cold Gas Dynamic Spraying of Tungsten Carbide-Nickel Coatings, *Met. Powder Rep.*, 2016, **71**, p 356–358
16. P. Nunthavarawong, N. Sacks and I. Botef, Effect of Powder Feed Rate on the Mechanical Properties of WC-5 wt%Ni Coatings Deposited Using Low Pressure Cold Spray, *Int. J. Refract. Met. Hard Mater.*, 2016, **61**, p 230–237
17. S.A. Aliokht, P. Manimunda, P. Vo et al., WC-Ni Composite Coating Deposited by Cold Spray, *Surf. Coat. Technol.*, 2016, **308**, p 424–434
18. P. Nunthavarawong, N. Sacks and I. Botef, Tribological Characterization of Nb Ion Implanted WC-5wt%Ni Cold Sprayed Coatings in Dry Sliding Contact, *Int. J. Refract. Met. Hard Mater.*, 2019, **85**, p 105067
19. X.Q. Jia, L. Kang, X.Y. Liu et al., High performance ultra-thin Niobium films for superconducting hot-electron devices, *IEEE Trans. Appl. Supercond.*, 2013, **23**, p 2300704
20. ISO 4287 geometrical product specifications (GPS) - surface texture: profile method - terms, definitions and surface texture parameters. ISO Stand. 1997:1-25
21. ASTM C1327 standard test method for Vickers indentation hardness of advanced ceramics. ASTM Stand. 2015:1-10
22. ISO 20502 fine ceramics (advanced ceramics, advanced technical ceramics) — determination of adhesion of ceramic coatings by scratch testing. ISO Stand. 2015:1-31
23. M.T. Laugier, Adhesion of TiC and TiN Coatings Prepared by Chemical Vapour Deposition on WC-Co-Based Cemented Carbides, *J. Mater. Sci.*, 1986, **21**, p 2269–2272
24. Y.X. Wang and S. Zhang, Toward Hard Yet Tough Ceramic Coatings, *Surf. Coat. Technol.*, 2014, **258**, p 1–16
25. B.D. Beake, V.M. Vishnyakov and A.J. Harris, Nano-Scratch Testing of (Ti, Fe)Nx Thin Films on Silicon, *Surf. Coat. Technol.*, 2017, **309**, p 671–679
26. NIST X-ray photoelectron spectroscopy database [Internet]. Maryland: National Institute of Standards and Technology USA (NIST); [cited 2017 Mar 16]. Available from: http://srdata.nist.gov/xps/Default.aspx/
27. K. Oyoshi, S. Hishita, K. Wada et al., Roughness Study of Ion-Irradiated Silica Glass Surface, *Appl. Surf. Sci.*, 1996, **100**(101), p 374–377
28. A. Ghabchi, M. Rombouts, K. Holmberg et al., Microstructure and Failure Modes During Scratch Testing of Laser Cladded WC-NiCrBSi Coatings with Spherical and Angular Carbides, *Tribol. Mater. Surf. Interfaces*, 2013, **7**, p 13–20
29. A. Ghabchi, S. Sampath, K. Holmberg et al., Damage Mechanisms and Cracking Behavior of Thermal Sprayed WC-CoCr Coating Under Scratch Testing, *Wear*, 2014, **313**, p 97–105